Supporting Information for

Seismotectonics of southern Haiti: A new faulting model for the 12 January 2010 M7 earthquake

Newdeskarl Saint Fleur, Nathalie Feuillet, Raphaël Grandin, Eric Jacques, Jennifer Weil-Accardo, and Yann Klinger

Institut de Physique du Globe de Paris, Sorbonne Paris Cité, Univ Paris Diderot, UMR 7154 CNRS, 1 rue Jussieu, F-75238 Paris CEDEX 05, France

Content of this file:

- Methodology for morphotectonics and geology (A)
- Methodology for geodetic inversion and Coulomb stress calculation (B)
- References of the text
- Figures S1-S11 with captions

A- Morphotectonics and geology. Figures S1-S5.

Method: Landsat satellite imagery, air photographs from the Haitian National Centre of Geospatial Information (CNIGS) (pixel: 30 cm), digital elevation models (DEM) (spatial resolution: 30 m (ASTER) and 1 m (LIDAR, from the Rochester Institute of Technology) are used to map faults cutting recent geological surface and exhibiting youthful morphology. Topographic profiles (extracted from DEMs) are used to determine large-scale deformations imparted by faulting. The detailed geometry of fault scarps or folds (strike, segmentation, bends, steps) is studied in map view to obtain information on fault kinematics. Field observations are combined to characterize such faults down to scales of a few metres. In the submarine part, we use available bathymetric charts (1:25000) to identify faults that continue underwater and to further constrain their geometry. Submarine fault scarps are mapped using perturbations of bathymetric gradients. Steep gradients between slope breaks allow fault throws to be estimated from orthogonal profiles.

B- The 2010 Haiti Earthquake static coseismic deformation and Coulomb stress changes. Figure S6-S11.

Measurements of the static deformation induced by the 2010 Haiti earthquake were derived from Interferometric Synthetic Aperture Radar (InSAR) and the Global Positioning System (GPS).

L-band SAR data was acquired by the PALSAR sensor on board of the ALOS satellite operated by the Japanese Aerospace Exploration Agency (JAXA). The data was made available thanks to the Supersites initiative [*http://supersites.earthobservations.org/haiti.php*]. A standard interferometric processing strategy was applied using the ROI_PAC and NSBAS softwares [*Doin et al.*, 2011; *Rosen et al.*, 2004]. Pre-processing of the ALOS-PALSAR data was achieved thanks to codes provided by Rob Mellors, David Sandwell and Zhenghong Li through the ROI_PAC wiki [*http://www.roipac.org/*]. Topographic phase was calculated with the Shuttle Radar Topographic Mission (SRTM) digital elevation model. Three ascending tracks (136, 137 and 138) and one descending track (447) were processed (Fig. S6 and S7). The resulting line-of-sight displacement maps are similar to those presented in previous studies [e.g., *Calais et al.*, 2010; *Hashimoto et al.*, 2011; *Hayes et al.*, 2010].

The GPS data used in this study is from Calais *et al.* [2010].

Slip model

- Inversion strategy

A formal inversion of the geodetic data set was performed to constrain the geometry of the faults that ruptured during the Haiti earthquake, together with the distribution of coseismic slip on these faults (Fig. S9). Ground deformation was modeled as the result of elastic deformation of a uniform, homogeneous half-space in response to uniform slip on several rectangular dislocations, using the analytical solutions of Okada [1985]. Prior to inversion, the InSAR data was decimated based on the distance from the inferred surface projection of the EPGF, using the method described in Grandin *et al*. [2009]. The weight of the InSAR data set with respect to the GPS data set was adjusted by attributing reasonable errors to each data set such that the final solution is a compromise between an InSAR-dominated and a GPS-dominated solution.

We have assumed that two faults (the Enriquillo-Plantain Garden Fault and the Lamentin Fault) were responsible for the observed deformation pattern. The inversion was performed in two steps. A first non-linear inversion of the optimal geometry of the fault planes (dip, strike, size, depth, location) was performed using an assumption of uniform slip, following the method of Tarantola and Valette [1982]. At this stage, we constrained the updip surface projection of the two faults to coincide with the mapped surface trace of the EPGF and the Lamentin Fault. Furthermore, the dip angle of the two dislocations (65° and 40° for EPGF and Lamentin Fault, respectively), were fixed to stabilize the inversion. In a second step, the fault planes with optimal geometry were discretized into a series of contiguous 2x2 km dislocations. The slip distribution was then determined by a least-squares inversion using the method described in Jónsson *et al*. [2002]. Spatial smoothing was achieved by a Tikhonov regularization using a discrete second-order spatial derivative of the slip distribution . The degree of smoothing imposed in the inversion was determined as a compromise between fit to the data and simplicity/compacity of the slip distribution, using an L-curve criterion (Fig. S8). Regularization was further enforced by restricting the rake angle to be within 90° of the a priori rake angle determined from the uniform slip solution. Orbital residuals were mitigated by simultaneously inverting for a first order polynomial surface for each InSAR data set.

Limits of the information provided by GPS data

The GPS benchmarks that recorded the 2010 Haiti earthquake are distributed unevenly with respect to the coseismic faults (Fig. S9). On one hand, most measurement sites are located >30 km away from the epicentral region. These distant measurements are mostly sensitive to the average focal mechanism of the earthquake source and to the seismic moment, but they are little sensitive to details of the rupture model [*Ziv et al.*, 2013]. On the other hand, three GPS benchmarks are located within an epicentral distance less than the fault characteristic length (DFRT, LEOG, TROU), which makes them extremely sensitive to the details of the rupture. However, this enhanced sensitivity mostly applies to the parts of the fault planes that are closer to them, whereas the influence of remote sectors of the fault planes is more reduced. A paradoxical consequence of this heterogeneous resolution is that an optimal fit to the data can only be achieved with a "rough" slip solution, since the overall RMS misfit is dominated by near-field measurements. Benchmark DFRT illustrates best this paradox. Indeed, DFRT appears to be located right above the main coseismic asperity of the 2010 Haiti earthquake [*Bilham and Fielding*, 2013]. Large slip magnitude on a restricted area of the fault plane in the few hundred metres below the benchmark is required to reproduce the large displacement at the surface (horizontal displacement equal to 64 cm, vertical displacement equal to 35 cm). On the other hand, the total seismic moment cannot be too large to explain the small displacements away from the epicentral region. Hence, it is difficult to explain displacement at DFRT using a simple "smooth" rupture model. Assuming that the measurement is correct, this likely indicates that coseismic displacement at this site is mostly sensitive to details on the rupture in the few kilometres below the surface, which probably include inelastic processes that are not accounted for by the model. Since the displacement at DFRT is larger by nearly two orders of magnitude than displacement at most stations located away from the epicentral region, the overall misfit to the GPS data set is heavily penalized by the difficulty to honour the displacement measured at DFRT. As a consequence, reconciling the displacements measured both in the near-field and at other, more distant sites, is virtually impossible as long as stringent smoothing constraints are implemented.

The goodness of the fit is presented in table 1.

Table 1: Goodness of fit for the preferred two-fault model of Figure 5 *

Data set	Number of data points	Standard deviation prior to inversion (cm)	Standard deviation of residual (cm)	(%)Var reduction
InSAR - T136	74	2.6	1.9	47
InSAR - T137	213	18.8	7.7	83
InSAR - T138	81	12.2	7.4	63
InSAR - T447	233	12.7	8.0	60
GPS East component	39	11.4	8.0	51
GPS East component	39	11.4	8.0	51
GPS Up component	39	10.0	1.9	96

* The standard deviation of each data vector prior to the inversion is provided in column 3 (RMS_{prior}), whereas the standard deviation of each residual vector after subtraction of predicted displacements is provided in column 4 ($RMS_{residual}$). The percentage of variance reduction is computed according to the formula $(1-[RMS_{residual}/ RMS_{prior}])*100$. A map view of the fit to individual InSAR data sets can be found in Figures S5 and S6, while the fit to the GPS vectors is plotted in Figure S9.

Coastal uplift

A quantitative assessment of the coseismic deformation of the shoreline during the 2010 Haiti earthquake has been reported by Hayes *et al*. [2010] and Weil-Accardo [2011] using a comparison of the post-earthquake sea level and the elevation of coral reef terraces that were active before the earthquake (Fig. S10). This data shows a generally good agreement with the vertical deformation pattern deduced from InSAR, including a site of maximum uplift (>50 cm) on the western edge of the Léogâne Delta Fan [*Hayes et al.*, 2010]. However, the uplift pattern caused by the coseismic static deformation is superimposed on a complex pattern of subsidence induced by extensive occurrence of lateral spreading along the coast. Therefore, individual measurements of coastal uplift derived from coral observations are prone to large uncertainties. We have computed the predicted vertical displacement for the coral sites reported by Hayes *et al*. [2010] in order to assess the compatibility of our solution with available coastal uplift observations. We find that the overall pattern is well captured by our solution, although coral uplift data was not used in the inversion (Fig. S10). The only exceptions are the sites located at the western and eastern terminations of the rupture. Observations at the five sites located at the western end of the rupture highlight an incoherent pattern, with vertical displacements of up to +/- 25 cm, whereas the model predicts ~10 cm uplift for all five sites. Regarding the easternmost surveyed point ("Passion beach"), our model predicts an uplift of ~40 cm, in agreement with InSAR, while the uplift deduced from reported coral reef observations is only 7 cm. A similar disagreement between observations and InSAR-derived models for these specific sites is reported by Hayes *et al*. [2010] and Meng *et al*. [2012].

Coulomb stress change

Static stress change induced by the 2010 Haiti earthquake was modeled using the distributed slip model determined from the joint GPS-InSAR inversion, using the analytic solutions provided by Okada [1992]. A static friction coefficient of 0.4 and a shear modulus of 33 GPa were used throughout.

First, in order to assess the viability of the stress transfer model, we computed the Coulomb stress change induced by slip on the Lamentin sub-fault, with stress change being resolved on the Enriquillo-Plantain Garden sub-fault. The optimal slip direction on the Enriquillo-Plantain Garden sub-fault was determined as the direction of slip that maximizes the magnitude of the Coulomb stress function (Fig. S11).

Second, in order to investigate the possible response of neighboring faults to the Haiti earthquake, we calculated the Coulomb stress function for prescribed mechanisms representative of the two main families of active faults in Hispaniola (Fig. 5): (1) WSW-ENE striking, 65° north-dipping, strike-slip faults, similar to the EPGF, and (2) WNW-ESE striking, 40° south-dipping, reverse faults, similar to the Lamentin Fault. A depth of 7.5 km was assumed for the calculation, which corresponds to the mid-depth of the seismogenic layer.

References

Armijo, R., P. Tapponnier, J. Mercier, and T. L. Han (1986), Quaternary extension in southern Tibet: Field observations and tectonic implications, *Journal of Geophysical Research: Solid Earth (1978–2012)*, *91*(B14), 13803-13872.

Bilham, R., and E. Fielding (2013), Remote sensing and the search for surface rupture, Haiti 2010, *Nat Hazards*.

Calais, E., A. Freed, G. Mattioli, F. Amelung, S. Jónsson, P. Jansma, S.-H. Hong, T. Dixon, C. Prépetit, and R. Momplaisir (2010), Transpressional rupture of an unmapped fault during the 2010 Haiti earthquake, *Nature Geoscience*, *3*, 794-799.

Doin, M.-P., S. Guillaso, R. Jolivet, C. Lasserre, F. Lodge, G. Ducret, and R. Grandin (2011), Presentation of the small-baseline NSBAS pro- cessing chain on a case example: The Etna de- formation monitoring from 2003 to 2010 using ENVISAT data, *Proceedings of the European Space Agency Symposium "Fringe"*, 303–304.

Grandin, R., A. Socquet, R. Binet, Y. Klinger, E. Jacques, J. B. de Chabalier, G. King, C. Lasserre, S. Tait, and P. Tapponnier (2009), September 2005 Manda Hararo-Dabbahu rifting event, Afar (Ethiopia): Constraints provided by geodetic data, *Journal of Geophysical Research: Solid Earth (1978–2012)*, *114*(B8).

Hashimoto, M., Y. Fukushima, and Y. Fukahata (2011), Fan-delta uplift and mountain subsidence during the Haiti 2010 earthquake, *Nature Geoscience*, *4*(4), 255-259.

Hayes, G., R. Briggs, A. Sladen, E. Fielding, C. Prentice, K. Hudnut, P. Mann, F. Taylor, A. Crone, and R. Gold (2010), Complex rupture during the 12 January 2010 Haiti earthquake, *Nature Geoscience*, *3*(11), 800-805.

Jónsson, S., H. Zebker, P. Segall, and F. Amelung (2002), Fault slip distribution of the 1999 Mw 7.1 Hector Mine, California, earthquake, estimated from satellite radar and GPS measurements, *Bulletin of the Seismological Society of America*, *92*(4), 1377-1389.

Meng, L., J.-P. Ampuero, A. Sladen, and H. Rendon (2012), High-resolution backprojection at regional distance: Application to the Haiti M7.0 earthquake and comparisons with finite source studies, *Journal of Geophysical Research*, *117*, 1-16.

Okada, Y. (1985), Surface deformation due to shear and tensile faults in a half-space, *Bulletin of the seismological society of America*, *75*(4), 1135-1154.

Okada, Y. (1992), Internal deformation due to shear and tensile faults in a half-space, *Bulletin of the Seismological Society of America*, *82*(2), 1018-1040.

Rosen, P. A., S. Hensley, G. Peltzer, and M. Simons (2004), Updated repeat orbit interferometry package released, *Eos, Transactions American Geophysical Union*, *85*(5), 47-47.

Tarantola, A., and B. Valette (1982), Generalized nonlinear inverse problems solved using the least squares criterion, *Reviews of Geophysics*, *20*(2), 219-232.

Weil-Accardo, J. (2011), Vertical deformations related to the January 12 2010 Haïtiearthquake, paper presented at Conférence Géologique de la Caraïbe.

Ziv, A., M. P. Doin, and R. Grandin (2013), What can be learned from underdetermined geodetic slip inversions: the Parkfield GPS network example, *Geophysical Journal International*.

Figures with captions:

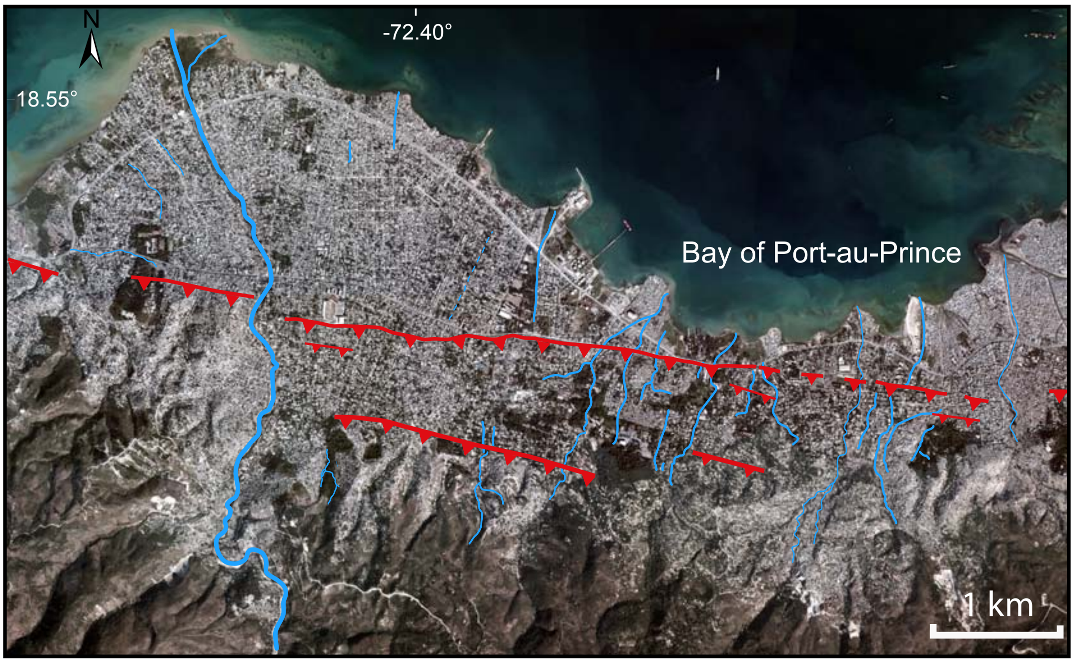

Figure S1: The Lamentin thrust across the heart of the densely populated city of Carrefour. The active Lamentin thrust system emerges in the heart of the city of Carrefour (data: aerial photograph of 30 cm of spatial resolution, resized into 1 m).

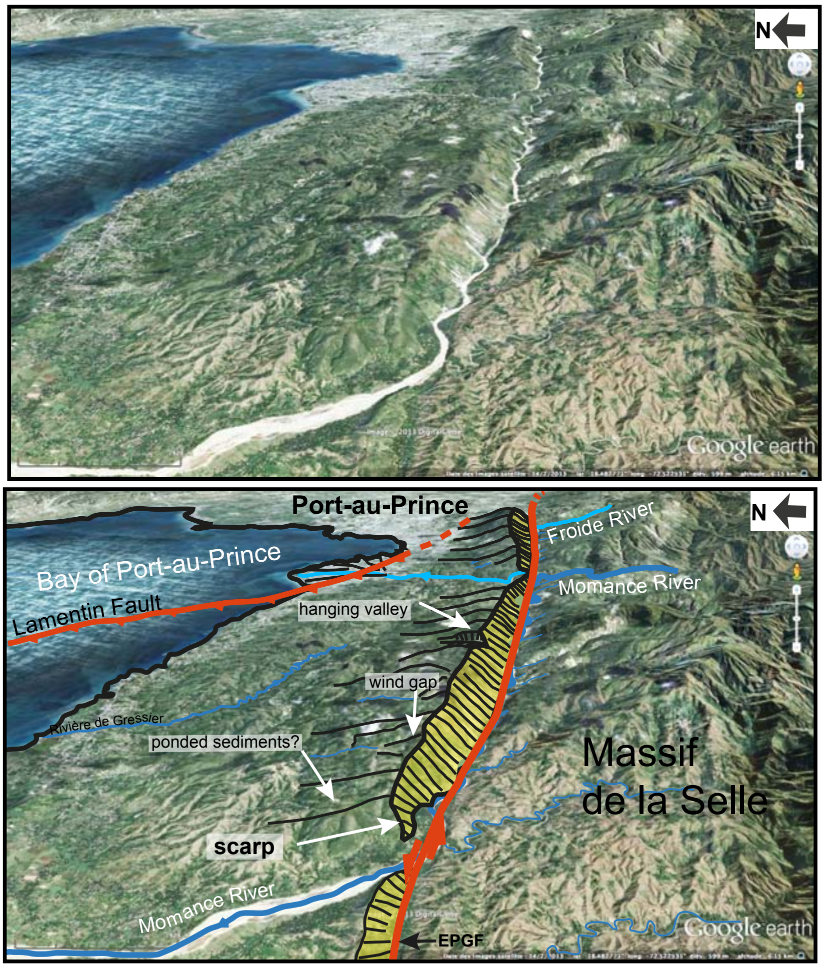

Figure S2: Geomorphic markers of on-going uplift north of the EPGF. a) The sharp uphill-facing Enriquillo Plantain Garden Fault scarp is incised by numerous small, narrow, intermittent gullies, some flowing in perched wineglass valleys, implying that transverse stream incision has not kept pace with relative tectonic uplift [*Armijo et al.*, 1986]. b) Northeastward view on a part of the crustal block uplifted between the EPGF and the Lamentin Fault. The image was elaborated using aerial photograph (with a spatial resolution of 30 cm) superimposed on ASTER topography (spatial resolution: 30 m) with no vertical exaggeration. Perched alluvial terraces deeply incised by canyons attest for uplift of the crustal block. In addition, numerous wind gaps, ponded sediments, upstream of deep gorges incised by streams flowing towards the bay of Port-au-Prince may indicate a drainage reversal due to tectonic uplift.

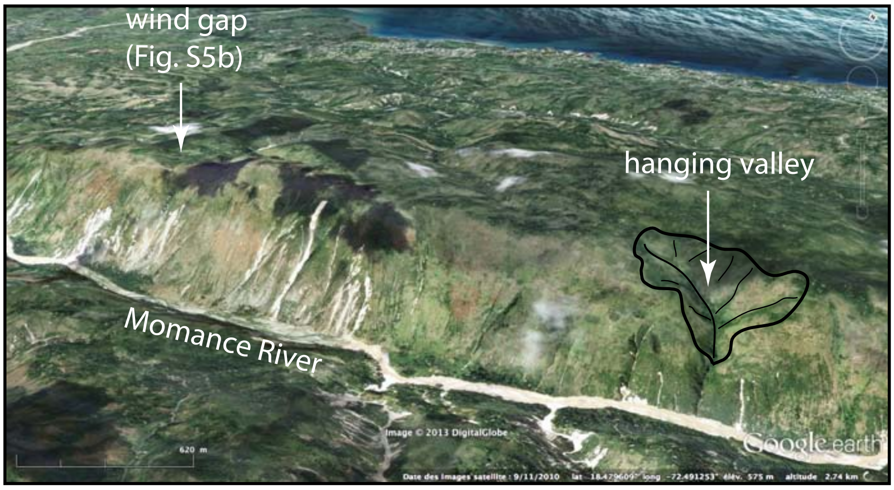

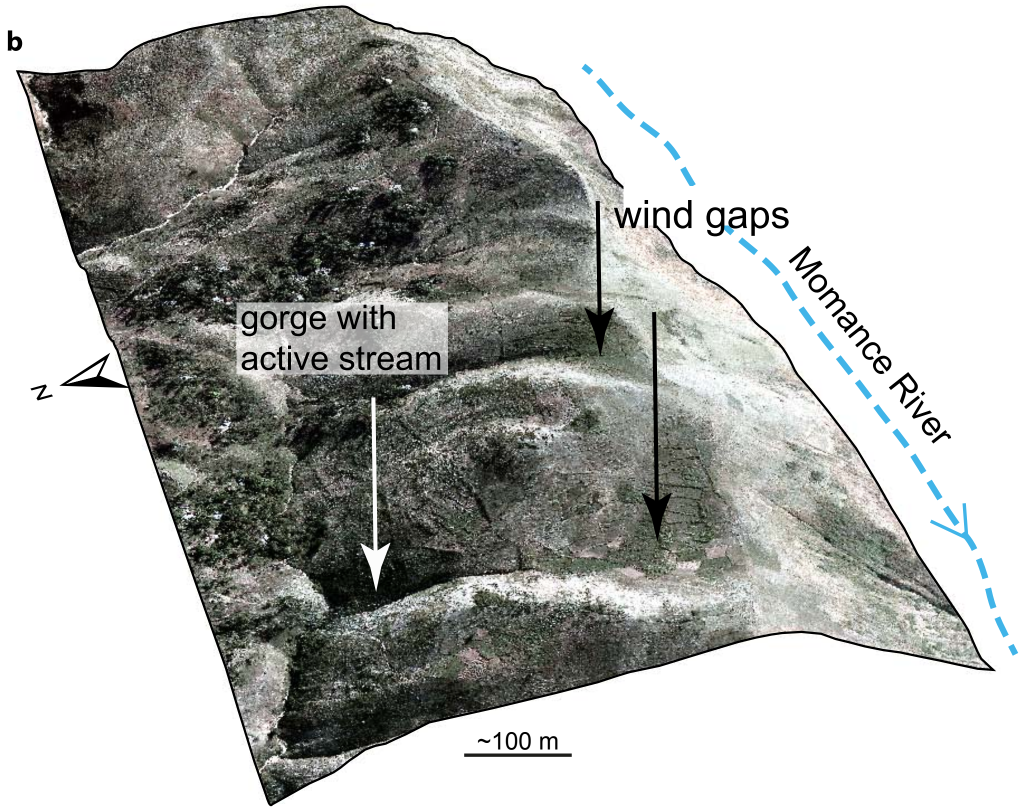

Figure S3: Eastward view of the EPGF scarp. a) Google Earth 3D eastward view of the Rivière Momance and the Rivière Froide Valleys and interpretation. The Enriquillo-Plantain Garden Fault and the Lamentin thrust bound an uplifting block which is limited to the south by a ~35 km long, up to 700 m high, linear and steep uphill-facing scarp (in yellow in b). The scarp acts as a shutter ridge blocking the drainage and diverting the main rivers (Momance and Froide, in blue).

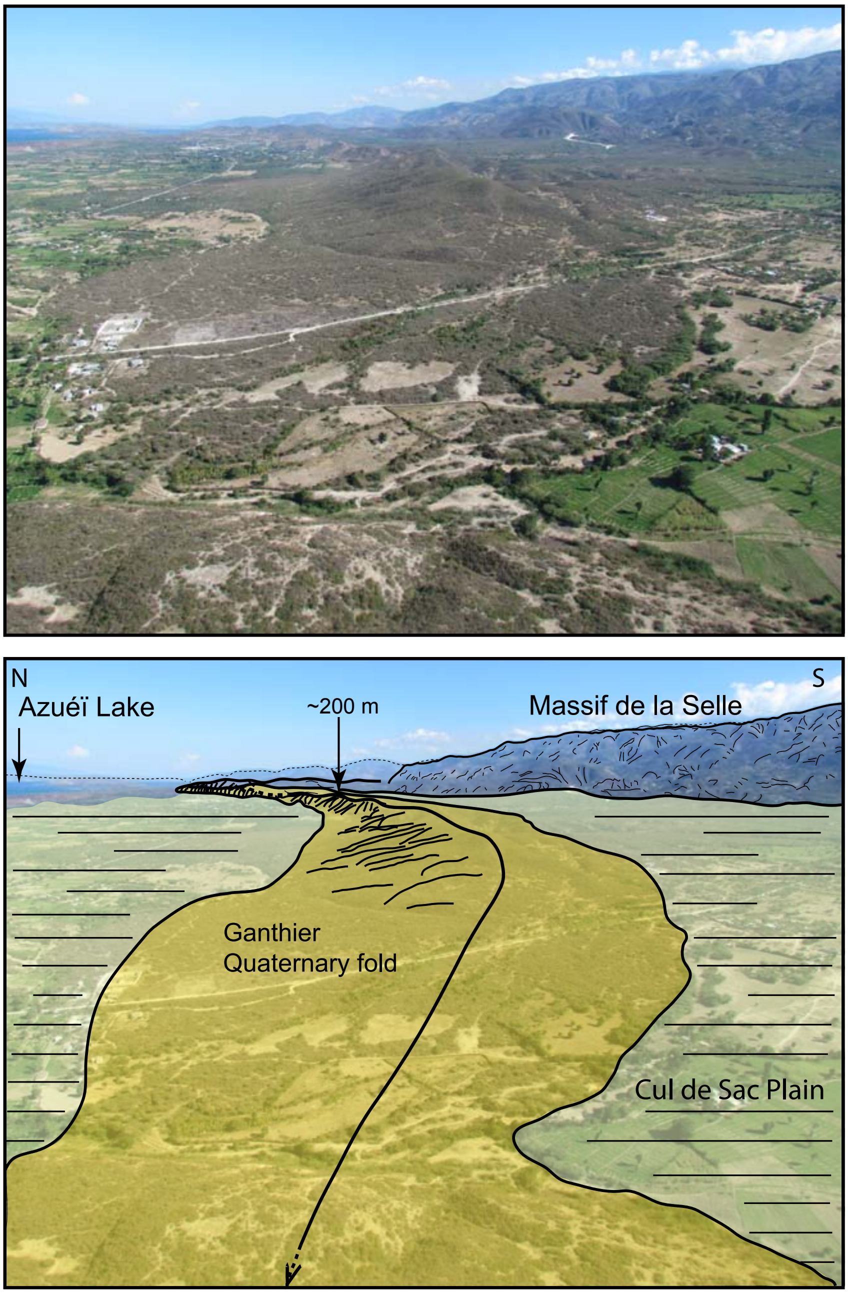

Figure S4: Eastward view of the Ganthier Fold and interpretation. This photograph taken in 2012 from a helicopter shows the Quaternary Ganthier Fold.

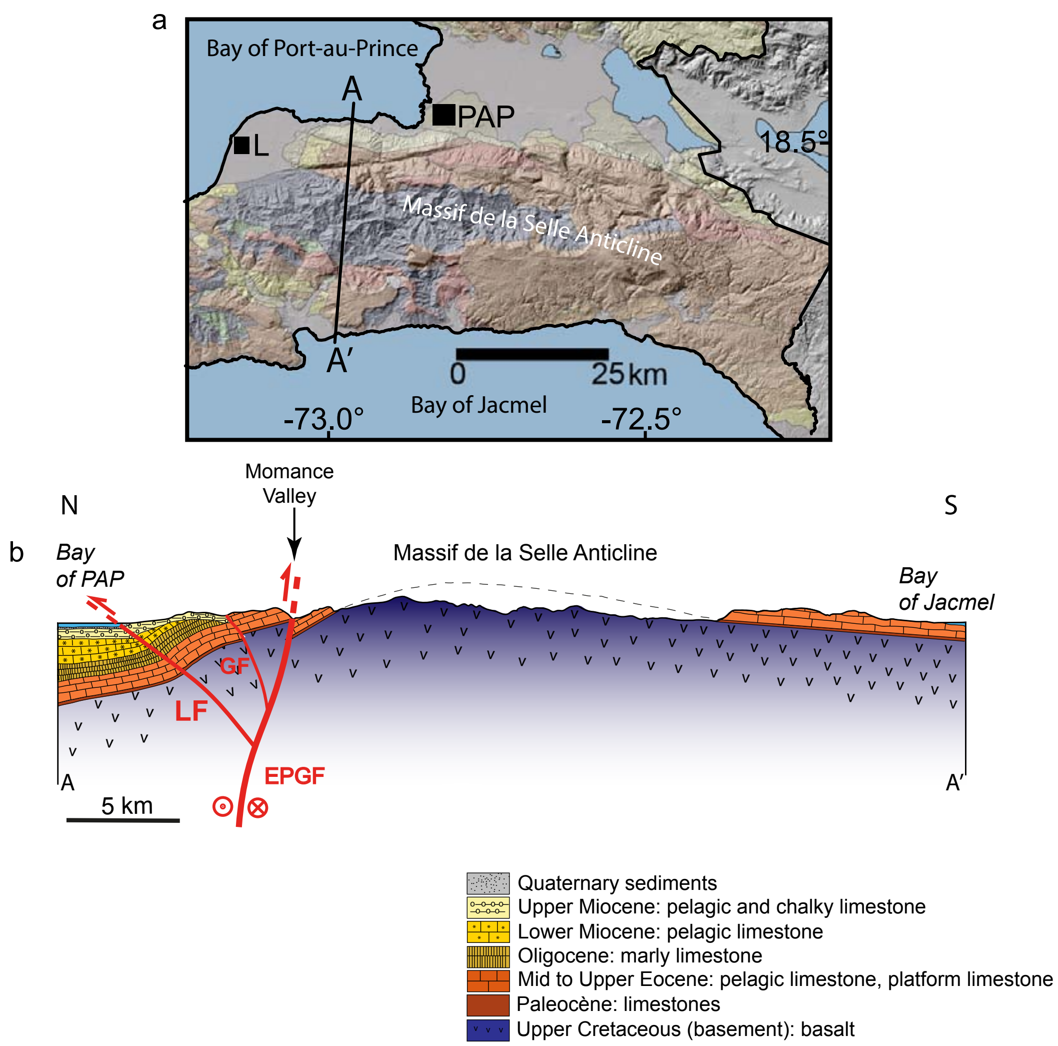

Figure S5: N-S Geological cross-section perpendicular to the Enriquillo Plantain Garden (EPGF) and Lamentin Fault system. a) The 1/250000 geological map [*http://www.bme.gouv.ht/*] is superimposed to the ASTER topography (30 m of spatial resolution) illuminated from the NW. PAP, Port au Prince; L, Léogâne. Black line with letters: location of the topographic and geological cross-section shown in b). b) N-S geological cross-section across the Southern Peninsula of Haiti between the bays of Port-au-Prince (PAP) and Jacmel showing the geometry of the EPGF-Lamentin Fault system at depth (with no vertical exaggeration). This fault system crosscuts and uplifts the north flank of the Massif-de-la-Selle Anticline. EPGF, Enriquillo-Plantain Garden Fault ; GF, Gressier Fault; LF, Lamentin Fault.

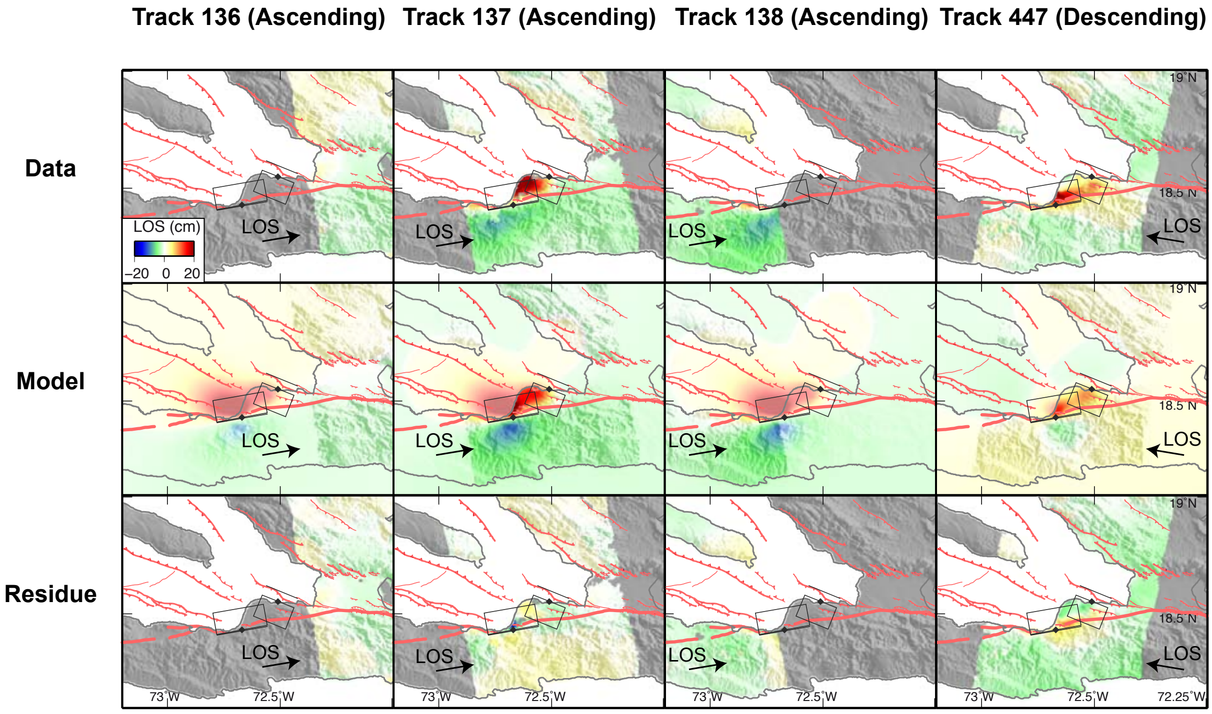

Figure S6: (top row) observations of coseismic deformation derived from InSAR for the four available acquisition geometries, (middle row) modeled deformation and (bottom row) residual deformation.

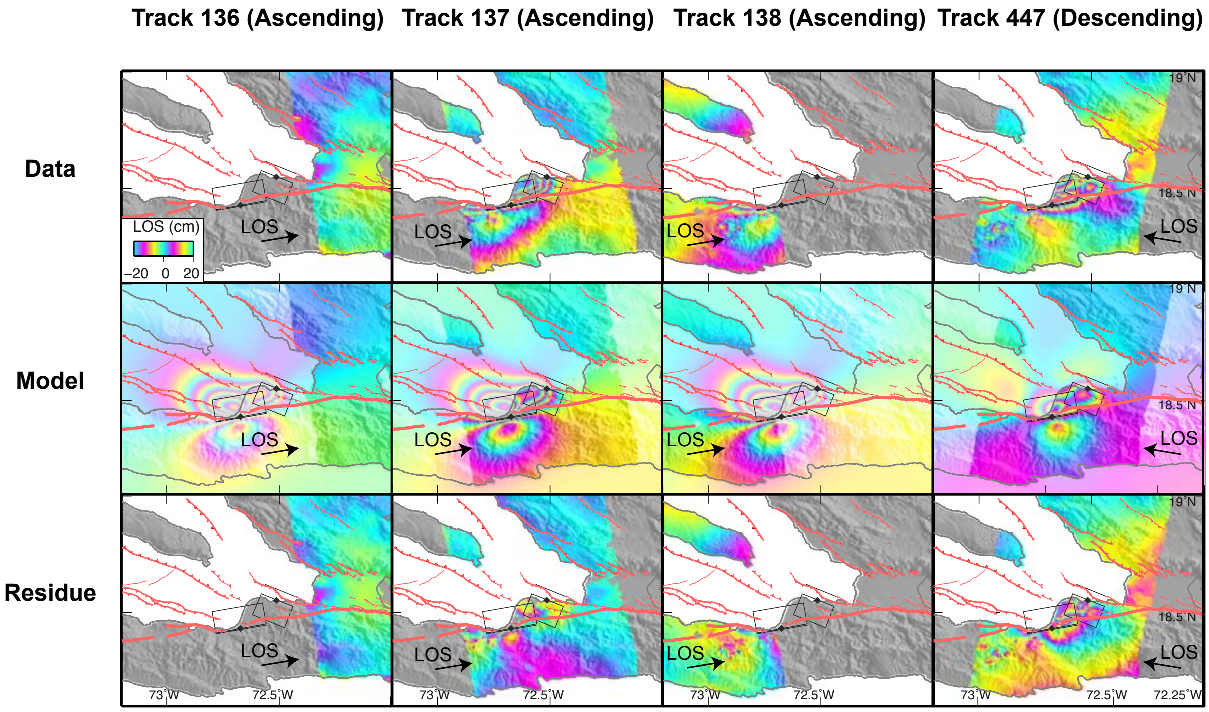

Figure S7: Same as Fig. S1, except that a cyclic colour palette is used.

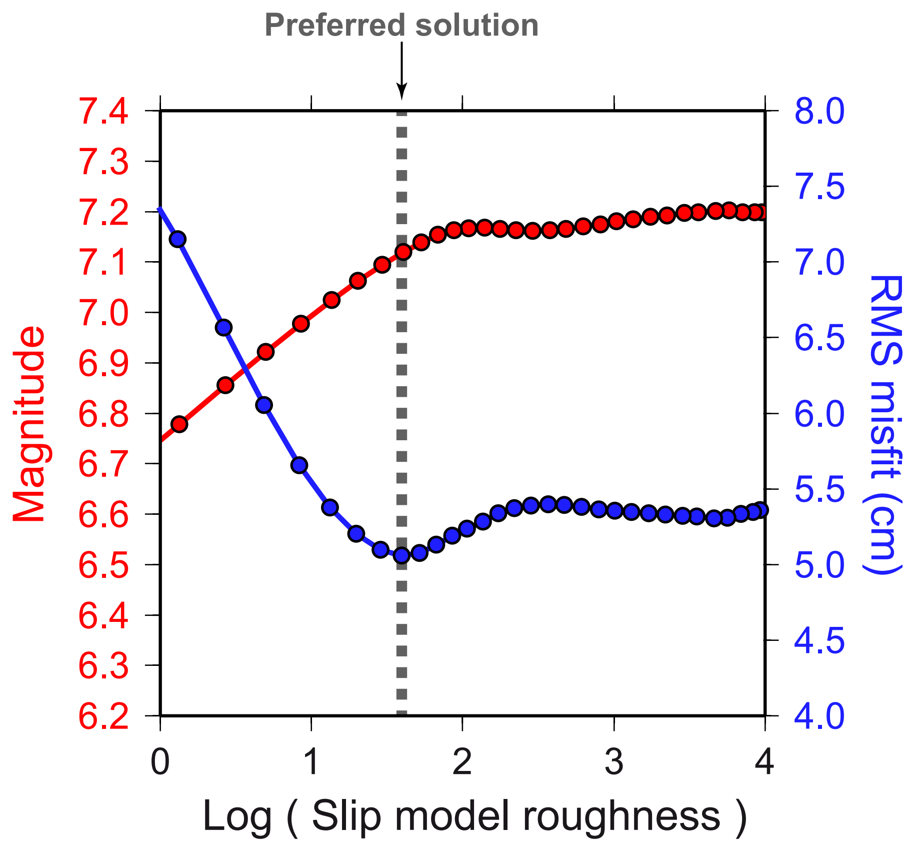

Figure S8: L-curve representation of the trade-off between imposed slip distribution roughness and misfit to the data (in blue). The magnitude corresponding to each tested solution is indicated in red. Small values of model roughness (to the left) correspond to an excessive smoothing, which does not allow the solution to capture the full complexity of the geodetic data. Conversely, large values of model roughness (to the right) correspond to "spiky" solutions including numerous distinct patches of significant slip that do not improve the fit to the data. The preferred solution is indicated by the vertical dashed grey line.

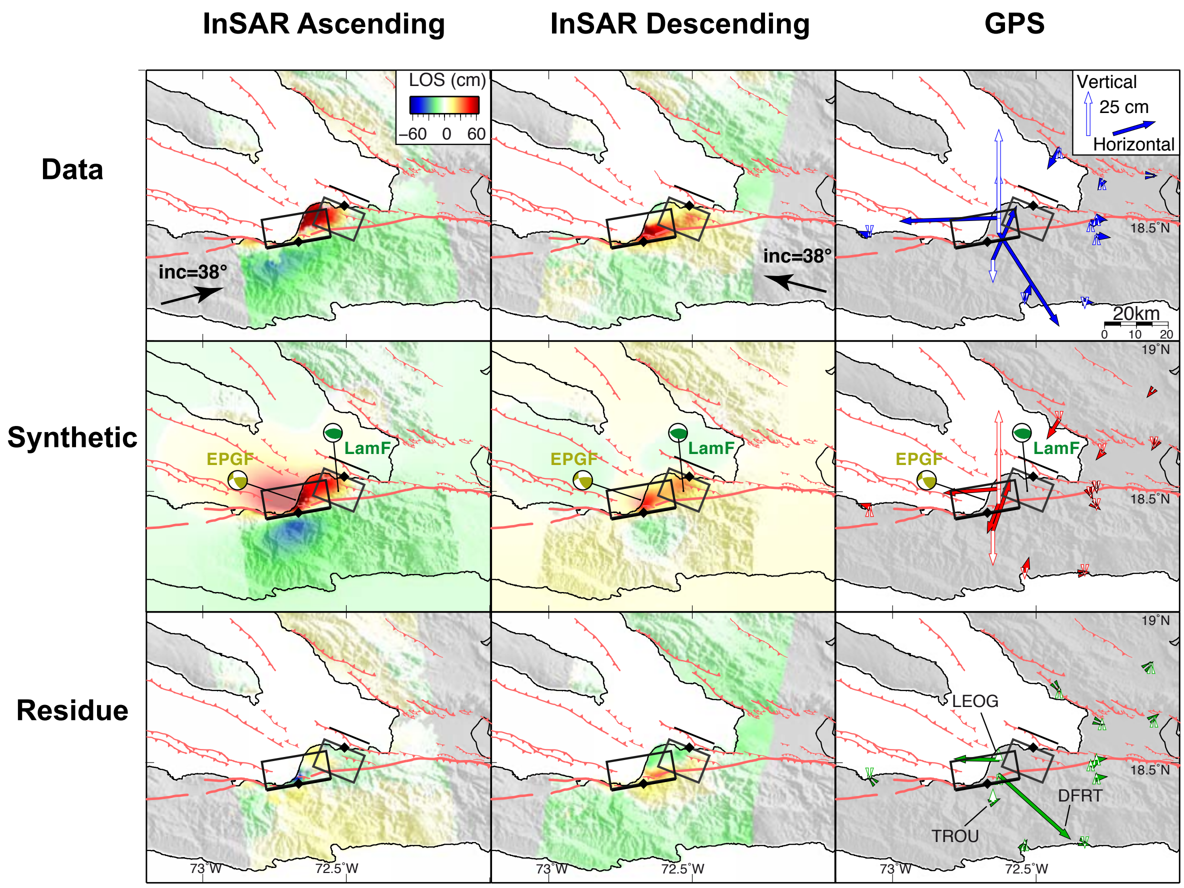

Figure S9: a. Top row: GPS and InSAR measurements of ground deformation for the 2010 Haiti earthquake. The left and middle columns show the InSAR data acquired on the ascending and descending track, respectively, with the black arrow indicating the direction of the satellite line-of-sight (LOS). Motion away or toward the satellite is indicated using blue and red shading, respectively. In the right column, the vertical and horizontal components of GPS-derived displacement are indicated by white-filled and colour-filled arrows, respectively. Black rectangle indicate the projection of the edges of the dislocations at the surface, with the black diamonds marking the middle of the upper edge of the dislocations. Middle row: Deformation is modeled as the result of slip on the EPGF, in yellow (strike=260° ; dip=65° ; average rake=33° ; seismic moment = 4.65×10^{19}Nm) and on the Lamentin fault, in green (strike=112° ; dip=40° ; average rake=111° ; moment = 2.36×10^{19}Nm). The focal mechanisms indicate the average moment tensor for each fault plane. The model shows a maximum uplift of about 50 cm of the Léogâne Delta Fan, consistent with the coral data acquired right after the event (b) [*Hayes et al.*, 2010] (see S10). Bottom row: Residual displacements (data minus model). Significant residual horizontal displacement at DFRT and LEOG is interpreted as the result of (1) near-fault superficial anelastic processes not accounted for in the modeling, (2) a likely oversimplification of the modeled fault geometry, (3) the assumed high degree of smoothness of the slip distribution, (4) or a combination thereof.

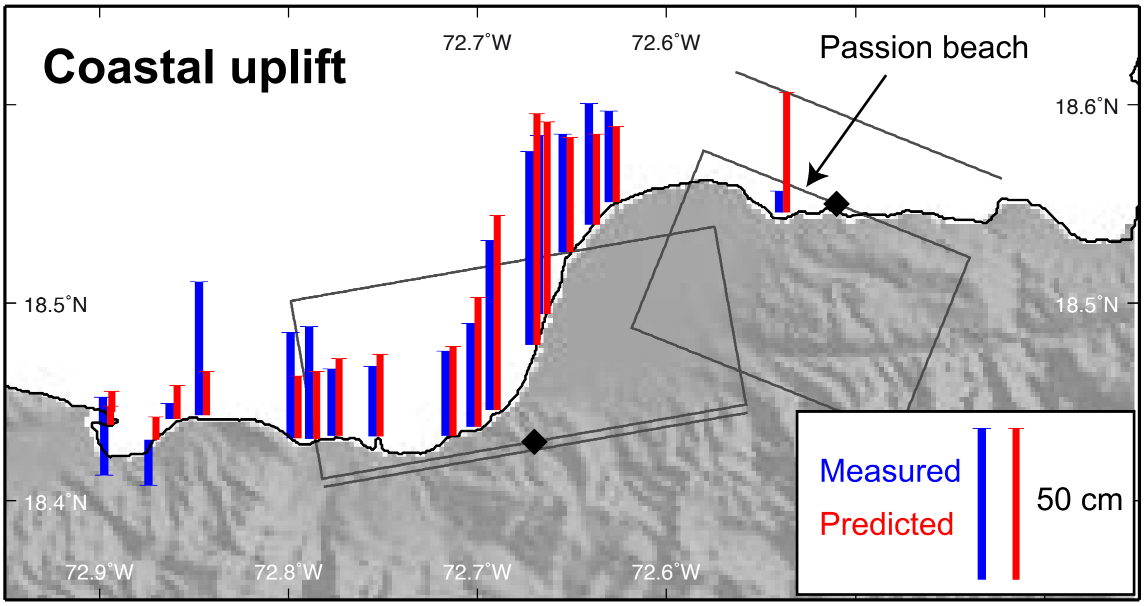

Figure S10: Coastal uplift reported by Hayes *et al.* [2010] (in blue), and predicted by the solution determined from this study (in red).

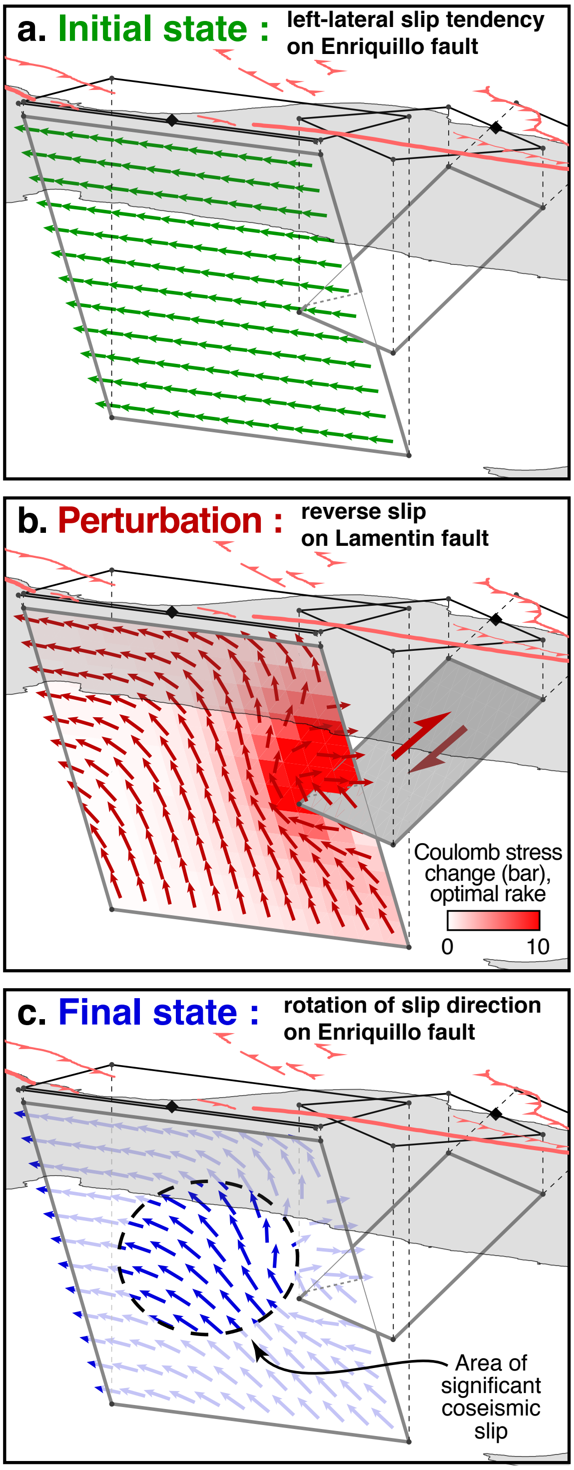

Figure S11: Rupture scenario of the 2010 Haiti event. a) Regional stress is assumed to promote an initial tendency for strike-slip on the EPGF. Arrows indicate the motion of the hanging-wall. b) Reverse slip on the Lamentin Fault during the initiation of the 2010 earthquake induces a static increase of the Coulomb stress on the EPGF. Red shading indicates the magnitude of the Coulomb stress increase, while red arrows show the direction of the optimal slip direction induced by slip on the Lamentin Fault. Here, a shear modulus of 33 GPa, a Poisson ratio of 0.25 and a static friction coefficient of 0.4 are used. c) Blue arrows indicate the result of the combination of the regional-induced slip strike-slip tendency on the EPGF and the perturbation induced by reverse slip on the Lamentin Fault. The blue arrows are obtained by adding the "regional" vector field in a. with the "perturbation" vector field in b. (the latter being multiplied by the intensity of the Coulomb stress change in b). The magnitude of the "regional" vector field is adjusted so that both vector fields have similar magnitude in the area of influence of the Lamentin Fault.